Opt Quant Electron (2016) 48:130
DOI 10.1007/s11082-015-0365-1

Diffuse optical imaging through incorporating structural information into edge-preserving regularization

Liang-Yu Chen[1,2] · **Min-Cheng Pan**[3] · **Jhao-Ming Yu**[2] · **Min-Chun Pan**[1,2]

Received: 27 August 2015 / Accepted: 29 December 2015 /

Abstract Diffuse optical imaging (DOI) is emerging as a new functional imaging modality that can be used for breast cancer screening. Due to the ill-posed inverse problem for DOI image reconstruction, regularization is essential to remedy such a drawback. In our previous study, we have successfully implemented edge-preserving regularization into image reconstruction algorithm for improving the reconstructed images. In this study, we incorporate additional anatomical image, which can be obtained from other imaging modality such as mammography or magnetic resonance imaging, although showing no tumor information, into edge-preserving regularization for further improving the reconstructed images. Reconstruction results show that the quality of reconstructed images can be significantly improved.

Keywords Diffuse optical imaging · Edge-preserving regularization · A priori information

---

This article is part of the Topical Collection on Micro/Nano Photonics for the International Year of Light 2015.

Guest Edited by Yen-Hsun Su, Lei Liu, Xinlong Xu and Zhenhua Ni.

✉ Min-Chun Pan
pan_minc@cc.ncu.edu.tw

[1] Graduate Institute of Biomedical Engineering, National Central University, No. 300, Jhongda Rd., Jhongli District, Taoyuan City 32001, Taiwan, R.O.C.

[2] Department of Mechanical Engineering, National Central University, No. 300, Jhongda Rd., Jhongli District, Taoyuan City 32001, Taiwan, R.O.C.

[3] Department of Electronic Engineering, Tung-Nan University, No. 152, Sec. 3, Beishen Rd., Shenkeng District, New Taipei City 222, Taiwan, R.O.C.

1 Introduction

Breast cancer is a common disease that occurs in women worldwide. According to the report from World Health Organization (2015), breast cancer is common leading causes of death to women. Therefore, it is demanding for a screening or diagnostic tool that enables to detect breast cancer effectively. Diffuse optical imaging (DOI) is emerging as a technique that aims for the purpose (Fantini and Sassaroli 2012; Durduran et al. 2012). DOI uses near infrared light to illuminate the breast, and reconstructs the distribution of chromophore concentrations (hemoglobin, water, and lipid) from the detected optical signals, which are in turn associated with features that bear diagnostic potential. The research results show that cancerous tissue is associated with higher hemoglobin and water concentrations, and a lower lipid concentration with respect to normal breast tissue (Cerussi et al. 2006; Choe et al. 2009). Moreover, instruments for DOI are comparatively cost-effective as compared with other instrumentation used conventionally for breast screening and/or diagnosis, such as X-ray mammography, magnetic resonance imaging (MRI), and breast ultrasound (US). Unfortunately, tissue scattering intrinsically limits the spatial resolution of DOI.

Apart from DOI concerned with functional state of breast for cancer detection, mammography, MRI, and breast US have been used primarily for anatomical imaging. X-ray mammography has been extensively applied in hospitals, because sufficient evidence shows that mammography screening contributes to substantial reductions in breast cancer mortality (Tabar et al. 2003); however, it is hampered by false positives and negatives (Elmore et al. 1998; Huynh et al. 1998), and sensitivity declines significantly with increasing breast density (Kolb et al. 2002), resulting in a need for providing clinically viable adjuncts to mammography. Breast MRI is a relatively recent diagnostic tool as an adjunct to mammography. It has the advantages of providing a three-dimensional view of breast with high sensitivity in dense breast tissue and, contrast to mammography, using non-ionizing radiation. The significant disadvantages of MRI include moderate specificity and high cost for routine screening (Hylton 2005). Breast US examination is also performed as supplemental second-line screening procedure in the population of women with mammographically dense breast tissue, which has been identified as an independent marker strongly associated with breast cancer risk (Nothacker et al. 2009). Data interpretation, however, strongly relies on operator's experience.

Due to the limitation and advantages of varied imaging modalities, combining DOI with mammography (Li et al. 2003; Fang et al. 2011; Collettini et al. 2012; Michaelsen et al. 2012; Fang et al. 2009; Krishnaswamy et al. 2012), MRI (Zhao et al. 2015; Brooksby et al. 2004; Boverman et al. 2005; Brooksby et al. 2005; Brooksby et al. 2006; Yalavarthy et al. 2007; Azar et al. 2007), or breast US (Chen et al. 2001; Zhu et al. 1999; Zhu and Chen 2003; Zhu et al. 2008) is showing promise for tumor detection by merging complementary functional and structural information into a single approach. It is anticipated that multimodality imaging may contribute to increase the screening/diagnostic effectiveness when distinct and complementary physiological data are available; and further, anatomical images can be used as a priori knowledge in the reconstruction algorithm to remedy the ill-posed inverse problem of DOI, and to improve the reconstructed images. The most straightforward way to combine a priori structural information into the DOI reconstruction procedure is to assume that optical property perturbation comes from the region of interest (ROI) shown in the anatomical image. Under this condition, the image reconstruction is just limited to the ROI (Chen et al. 2001); besides, regularization parameters that control the degree of regularization in the background and tumor, respectively, can be chosen differently to improve image resolution (Li et al. 2003). Another approach to applying a priori knowledge of the size and location of the heterogeneity in the reconstruction is to divide the whole medium into varied types of tissue (lipid, glandular tissue, and tumor), and each tissue type is assumed homogeneous within the defined regions during reconstruction. In this way, known as hard prior, the number of unknown in the inverse problem is greatly reduced (Krishnaswamy et al. 2012; Zhao et al. 2015; Brooksby et al. 2004; Boverman et al. 2005; Zhu et al. 1999). As being too rigidly enforced in the DOI image reconstruction process of hard prior, a variant approach, known as soft prior, was proposed to apply a priori knowledge of breast composition/tissue distributions; for instance, a Laplacian-type regularization matrix linking locations with similar properties was applied in the reconstruction to minimize variation within each region (Brooksby et al. 2005; Brooksby et al. 2006; Yalavarthy et al. 2007). Finally, reconstruction can be performed by using a finer grid for lesion region and a coarse grid for the background tissue based on anatomical image, leading to the total number of unknowns the same order of total measurements, and the inverse problem less ill-posed (Zhu and Chen 2003; Zhu et al. 2008).

In the study we utilize anatomical images and present a modified edge-preserving regularization (EPR) with incorporation of a priori edge information. In our EPR scheme, auxiliary variable is introduced to make the manipulation of minimization problem more efficient (Chen et al. 2012; Chen et al. 2013). The auxiliary variable also plays the role of discontinuity marker and preserves the sharpness of the reconstructed images. To further improve the reconstruction computation for clinical trial, we incorporate a priori information on edge locations, where available edge locations can be inferred from the anatomical images obtained from other imaging modalities, such as MRI and mammography, even though the structural information shows no tumor size and location. Then, the edge locations can be used as a guide to expedite the reconstruction by modifying the discontinuity marker during the reconstruction steps. We use the synthesized data to validate its effectiveness, and demonstrate that our new method recovers tumor further accurately and preserves the sharpness of edge better than those obtained by conventional EPR. Numerical tests are given to show that the new method is a robust algorithm in terms of the accuracy and availability of edge locations.

The following sections first briefly describe the reconstruction algorithm of DOI; then introduce the modified EPR scheme incorporating with edge locations as a priori information. Finally, synthesized data sets are employed to show the merits of the proposed scheme.

2 Method

In this study, a model-based optical property reconstruction algorithm is employed. Here, the optical-property distribution inside the tissue to be imaged is reconstructed iteratively first by comparing the measured diffusion photon density data and the theoretical prediction based on the forward model, i.e. diffusion equation; and then, the optical properties (inverse solution) are obtained through a least squares minimization problem in which the optimization strategy is adopted with edge-preserving regularization due to its ill-posed nature of the inverse problem.

2.1 Forward problem in DOI

NIR light transporting in the tissue can be modeled by the diffusion equation (Durduran et al. 2012):

$$\nabla \cdot \kappa(r)\nabla\Phi(r,\omega) - \left[\mu_a(r) - \frac{i\omega}{c}\right]\Phi(r,\omega) = -S(r,\omega), \tag{1}$$

where $\Phi(r, \omega)$ is the photon density at position r when isotropic light source $S(r, \omega)$ with modulation frequency ω is launched into the tissue, and c is the speed of light in the tissue. The characteristics of tissue are described by the optical diffusion coefficient $\kappa(r)$ and absorption coefficients $\mu_a(r)$. Moreover, the optical diffusion coefficient $\kappa(r)$ is defined as

$$\kappa(r) = \frac{1}{3\left[\mu_a(r) + \mu_s'(r)\right]}, \tag{2}$$

where $\mu_s'(r)$ is the reduced scattering coefficient. For image reconstruction, diffusion equation needs to be solved (forward problem) at each iteration step, i.e., calculating the photon density for a given set of optical property within the tissue. In this study, the finite element method (FEM) is applied to Eq. (1) with a Robin (type-III) boundary condition to solve the forward problem.

2.2 Inverse problem in DOI

The goal of DOI is to estimate the distribution of the optical diffusion and absorption coefficients in tissue from one-dimensional boundary measurement. This estimation can be achieved by minimizing the data-model misfit difference between the measured diffusion photon density data Φ^M around the tissue boundary, and the calculated model data Φ^C from solving the forward problem with the current estimated optical properties (Chen et al. 2012):

$$\chi^2 = \sum_{i=1}^{N_M} \left[\Phi_i^C - \Phi_i^M\right]^2, \tag{3}$$

where N_M is the number of measurement data. Due to nonlinearity with respect to the optical properties, numerical way of obtaining the inverse solution for minimizing Eq. (3) is iteratively solving the following equation:

$$\begin{bmatrix} \dfrac{\partial\Phi^C}{\partial\mu_a} & \dfrac{\partial\Phi^C}{\partial\kappa} \end{bmatrix} \begin{pmatrix} \Delta\mu_a \\ \Delta\kappa \end{pmatrix} = \left(\Phi^M - \Phi^C\right), \tag{4}$$

or simply denoted as $J\Delta\chi = \Delta\Phi$, where J is the Jacobian matrix. However, solving Eq. (4) usually experiences with an ill-posed problem. Therefore, regularization is required to remedy such a situation. Edge-preserving described in the following is adopted in this study.

2.2.1 Edge-preserving regularization

In edge-preserving regularization (EPR), the inverse problem in DOI is formulated as minimization of the objective function composed of a residual term and a regularization term into which a potential function φ with edge-preserving properties is introduced (Chen et al. 2012; Chen et al. 2013):

$$Q_{Ep}(\Delta\chi) = \|J\Delta\chi - \Delta\Phi\|_2^2 + \lambda^2 \sum_l \sum_k \varphi\left[(D_l\Delta\chi)_k\right], \tag{5}$$

where the index k is in the lexicographical order, the index l may represent the horizontal, vertical, or diagonal direction, and λ is the regularization parameter that balances the residual term and the regularization term. The potential function φ in the regularization term of the objective function determines the regularization imposed on every value of the first-order difference $D_l\Delta\chi$ which is used to detect the discontinuities of the update vector $\Delta\chi$ in specific direction l. Due to nonlinearity shown when minimizing Eq. (5), it is proven that the original objective function Eq. (5) can be transformed into the following objective function:

$$Q_{Ep}^{*}(\Delta\chi) = \|J\Delta\chi - \Delta\Phi\|_2^2 + \lambda^2 \sum_l \sum_k \left\{(b_l)_k(D_l\Delta\chi)_k^2 + \varphi\left[(b_l)_k\right]\right\}, \tag{6}$$

where the auxiliary variable b is introduced by half-quadratic regularization capable of making minimization of Eq. (6) linear with respect to $\Delta\chi$.

A strategy to calculate the update vector $\Delta\chi$ for minimizing Eq. (6) is described in the following. First, $\Delta\chi^n$ is fixed at iteration step $n + 1$, and b^{n+1} is simply computed using the expression obtained from minimization of Eq. (6):

$$\left(b_l^{n+1}\right)_k = \arg\min_{(b_l)_k}\left\{Q_{Ep}^{*}\left(\Delta\chi^n, (b_l)_k\right)\right\} = \frac{\varphi'\left[(D_l\Delta\chi^n)_k\right]}{2(D_l\Delta\chi^n)_k}. \tag{7}$$

Then the new update vector $\Delta\chi^{n+1}$ is the solution obtained from minimization of Eq. (6) when b^{n+1} is fixed:

$$\Delta\chi^{n+1} = \arg\min_{\Delta\chi}\left\{Q_{Ep}^{*}\left(\Delta\chi^n, b^{n+1}\right)\right\} = \left(J^TJ + \lambda^2\Delta_{Ep}^{n+1}\right)^{-1} J^T\Delta\Phi, \tag{8}$$

where $\Delta_{Ep}^{n+1} = \sum_l D_l^T B_l^{n+1} D_l$ and $B_l^{n+1} = diag\left[(b_l^{n+1})_k\right]$. Finally, the optical property inside the tissue is estimated iteratively with solving alternately the update equations, i.e., Eqs. (7) and (8), until the stopping criteria being met.

Edge-preserving regularization algorithm presented here is a flexible reconstruction algorithm. This means that different weighting function $\varphi'(t)/2t(t = D_l\Delta\chi^n)$ can easily adopted and used for image reconstruction. For example, a generalized Lorentzian function, an exponential function, or a generalized total variation function can be incorporated into edge-preserving regularization algorithm (Chen et al. 2013). In this study, we use a generalized Lorentzian function as the edge-preserving weighting function

$$\frac{\varphi'(t)}{2t} = \frac{(\gamma^2)^m}{(\gamma^2 + t^2)^m}, \tag{9}$$

where γ and m are adjustable parameters to change the behavior of the edge-preserving weighting function. The use of such a generalized Lorentzian function apart from others is for its adaptive characteristics and better estimation of absorption-coefficient image concerning functional information derived from the absorption coefficients at multi-wavelength (Chen et al. 2013).

2.2.2 *Incorporating structural information into edge-preserving regularization*

The minimization problem in Eq. (5) seeks the solution that best fits the measured diffusion photon density data and preserves sharp edge in reconstructed images. From other imaging modality, structural information can be obtained for the objects to be imaged. The location of known edges obtained from the discontinuities in the structural images can be employed and incorporated as constraints during the reconstruction computation. For instance, if specific tissue types such as fatty, fibro-glandular and tumor tissue in the reconstruction domain are known, then the soft priori approach can be used to improve the reconstructed images with the help of a Laplacian-type matrix, which links all nodes in a particular type tissue (Brooksby et al. 2005; Brooksby et al. 2006; Yalavarthy et al. 2007). In this study, we utilized the a priori edge information derived from discontinuities in the structural images, and impose it to guide for the minimization of Eq. (5).

In the edge-preserving regularization, its weighting function $\varphi'(t)/2t(t = D_l \Delta\chi^n)$ is required to satisfy the condition that it strictly decreases on $[0, +\infty)$. It has implicitly made an assumption that a large value of the gradient t corresponds to an edge and preserves such an edge by assigning a small weight value b. Therefore, when additional structural or edge information can be obtained from other imaging modality, one can incorporate this a prior edge information into edge-preserving regularization through modifying the weight value b calculated by Eq. (7),

$$\left(b_l^{n+1}\right)_k^{New} = w_b \left(b_l^{n+1}\right)_k, \tag{10}$$

during each reconstruction step, where w_b controls the degree of weight value b on the node k. For the node k corresponding to the edge obtained from structural information, w_b is chosen in the range of null and unit for further reducing the weight value b and preserving an edge in the reconstructed image. Otherwise, w_b is chosen greater than unit for increasing the weight value b and smooth the reconstructed image. It is noted that from Eq. (9) the influence of the structural information can be adjusted by appropriately selecting the value of w_b.

3 Results and discussion

In this section, the proposed image reconstruction algorithm with edge-preserving regularization scheme and incorporated structural information is evaluated through synthesized optical properties; besides, reconstructions with using edge-preserving regularization without structural information are also presented as a comparison.

The test phantom is 80 mm in diameter, of which optical properties with $\mu_a = 0.01\ \text{mm}^{-1}$ and $\mu_s' = 1.0\ \text{mm}^{-1}$ are employed for the background medium. NIR illumination with 20 MHz modulated light and multiple measurement positions are used to extract (for simulation) or collect (for experimentation) boundary information for image reconstruction. More specifically, in the simulation and experiments, it is designated 16 equally-spaced NIR illumination positions and also 16 measurement locations around the circular boundary for out-emitted data to be acquired; and thus it yields a total of 256 amplitude and 256 phase-shift observations for the computation of μ_a- and μ_s'-image reconstruction. Finite-element forward solution using a mesh consisting of 4225 nodes and 8192 triangle elements with Robin (type-III) boundary condition is obtained to generate simulated data. A second mesh with 817 nodes and 1536 triangle elements is generated and employed in the inverse problem for image reconstruction. All the reconstructed images reported here are reconstructed initially from homogeneous optical properties. For all cases, 30 iterations are used during the inverse computation, and the stopping criterion, $\|\Phi^{n-1} - \Phi^n\|^2 / \|\Phi^n\|^2 < 10^{-3}$, is employed.

As mentioned above, a generalized Lorentzian function is used as the edge-preserving weighting function due to its flexibility to change its behavior through the adjustable parameter γ and m, even though varied weighting functions can be employed for the edge-preserving regularization. Here, the values of $\gamma = 0.0025$ and $m = 1$ are adopted in the proposed edge-preserving weighting function; moreover, the regularization parameter λ presented in the regularization methods controls the ratio of the regularization term relative to the residual term. For the cases presented here, the regularization parameter $\lambda = 2^{*} max[diag(J^T J)]$ appears to provide excellent reconstructed optical-property images from all simulated data.

3.1 Discontinuity marker: the auxiliary variable b in edge-preserving regularization

In the investigation of incorporating structural information into edge-preserving regularization, to high light the role of the auxiliary variable b in the preservation of edges is significant. Since its value at each node depends on the presence of an edge through the weighting function, b can be considered as a discontinuity marker. At each iteration step of the reconstruction, new discontinuity markers are computed (Eq. 7) and then taken into account for the computation of new estimation (Eq. 8).

For the illustration of discontinuity markers, an example of reconstruction with synthetic data is first presented. In this simulation, image reconstructions are conducted under idealized conditions with no measurement noise. The data used in the reconstruction are

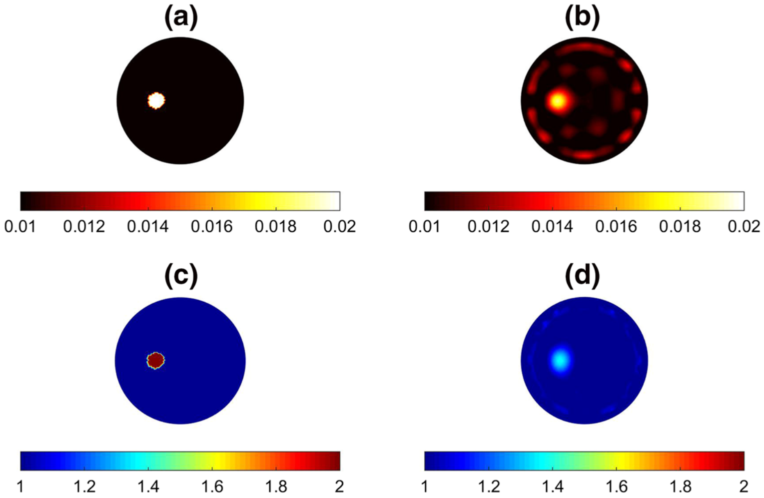

Fig. 1 Reconstruction of absorption and reduced scattering images with two-fold contrast level for an inclusion to the background. **a**, **c** are the designated absorption and reduced scattering images, respectively; and **b**, **d** are the corresponding reconstructed ones using edge-preserving regularization, but without incorporating structural information

obtained by the forward solution through the finite-element diffusion model with designated optical-property distribution, i.e. homogeneous background ($\mu_a = 0.01\ \mathrm{mm}^{-1}$ and $\mu_s' = 1.0\ \mathrm{mm}^{-1}$) embedded with a 10-mm-diameter inclusion, which is 20 mm off the center of the background. The optical properties of inclusion for both μ_a and μ_s' are assigned with two folds of the background, as shown in Fig. 1a, c for the absorption and reduced scattering coefficients, respectively. As a baseline for comparison, the reconstructed μ_a and μ_s' images, through using edge-preserving regularization without incorporating any structural information are illustrated in Fig. 1b, d; as shown, the inclusion can be reconstructed in this simple case. It is noted that the reduced scattering coefficient μ_s', adopted as a reconstruction parameter in an image formation algorithm, is actually inversely proportional to the diffusion coefficient κ (Eq. 2).

Figure 2 shows the evolution of both auxiliary variable and reconstructed absorption images in the first three iteration steps, where the auxiliary variable distributions are characterized in grey levels for better visualization. ‘b1’, ‘b2’ and ‘b3’ in Fig. 2 show the auxiliary variable distribution in the horizontal and two diagonal directions, respectively, ‘b’ is a simple summation of ‘b_1’, ‘b_2’, and ‘b_3’. In the present finite element model an interior node is surrounded by six neighboring nodes, as shown in the leftmost of Fig. 2, and thus these three directions are used for calculating the first-order difference of the current node and the neighboring node $D_l\Delta\chi$ (Eq. 7). It is noted that the auxiliary variable appears in darker grey near the inclusion boundary or edge due to its smaller weight value for preserving the edge during the computation, as describe in Sect. 2.2.2.

It can also be observed that all values of auxiliary variable are homogeneous at step 1 (first row of Fig. 2). It is reasonable since they are assigned from the designated values, a uniformly homogeneous. Then the first absorption image is reconstructed with b uniformly equal to the assigned value of 1. At step 2, new values of the auxiliary variables are computed using the first estimation (Eq. 7) and utilized to calculate the new estimation (Eq. 8), and so on. Note that other initial guesses of auxiliary variable could be used. However, using a homogeneous initial guesses allows important noise elimination during

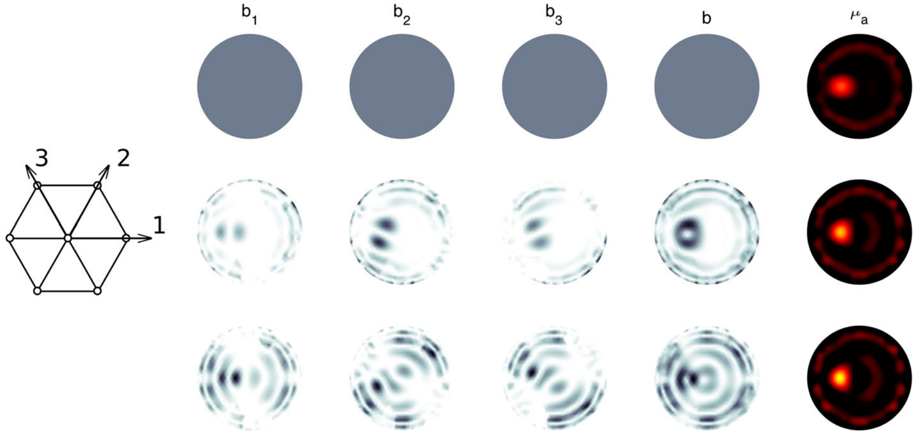

Fig. 2 Images of auxiliary variable in the three directions (noted in the direction of *1*, *2* and *3*), and their combination (a simple summation). The *upper*, *middle* and *lower rows*, respectively, show the auxiliary variable images and reconstructed absorption images at the 1st, 2nd, and 3rd iteration steps during the reconstruction of Fig. 1b

the first reconstruction step and explains the good results we obtain from the simulated data even though moderate noise was added.

The role of discontinuity maps played by the auxiliary variables clearly appears in Fig. 2. At each reconstruction step, discontinuities are introduced into the new estimation. The new discontinuity maps are computed from this new estimation and then introduced into the next estimation to generate sharper image. Therefore, when the discontinuity or edge information could be obtained from the structural image and incorporated into edge-preserving regularization algorithm, we could anticipate more superior reconstruction results.

3.2 Reconstruction with a priori information

The edge-preserving regularization incorporating structural information described in Sect. 2 was used to reconstruct images from synthetic data with 3 % Gaussian noise added in this section. Breast is a mix of adipose (fat) and fibro-glandular tissue. From coronal view of breast, adipose tissue composes an outer layer that surrounds the fibro-glandular tissue. Based on this anatomical structure, a two-layered phantom (Brooksby et al. 2005; Brooksby et al. 2006; Yalavarthy et al. 2007) with an inclusion embedded inside the inner layer (fibro-glandular) was used to evaluate the ability of this reconstruction technique resolving a more realistic structure in the simulation of breast imaging. The outer layer (fatty) has optical property values of $\mu_a = 0.01\ \mathrm{mm}^{-1}$ and $\mu_s' = 1.0\ \mathrm{mm}^{-1}$, and the inclusion (tumor) with $\mu_a = 0.04\ \mathrm{mm}^{-1}$ and $\mu_s' = 0.89\ \mathrm{mm}^{-1}$, was placed inside the inner layer (fibro-glandular) having the optical property values of $\mu_a = 0.02\ \mathrm{mm}^{-1}$ and $\mu_s' = 2.0\ \mathrm{mm}^{-1}$, as depicted in Fig. 3a, c. For the purpose of comparison, Fig. 3b, d show the reconstructed absorption and reduced scattering images using edge-preserving regularization without structural information incorporated. Apparently, the inclusion could be separated from inner layer in

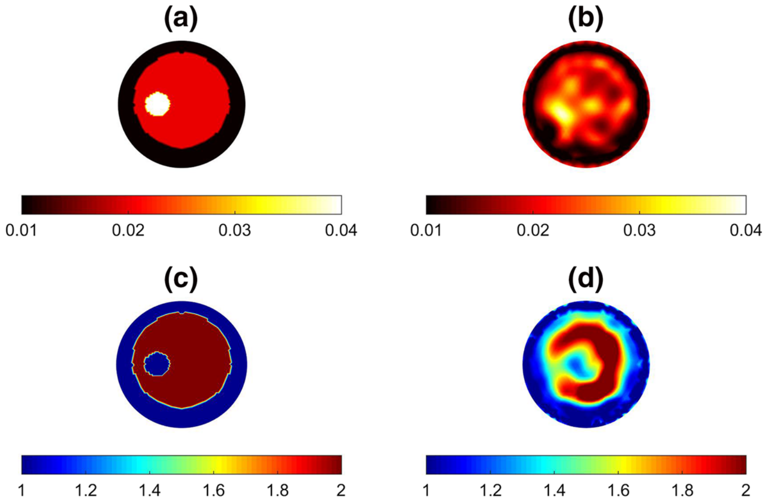

Fig. 3 Reconstruction of absorption and reduced scattering images for a phantom of layered domain with an inside inclusion. **a**, **c** are the designated absorption and reduced scattering images; **b**, **d** show the corresponding reconstructed images using edge-preserving regularization without incorporating structural information (3 % Gaussian noise added)

absorption image. However, due to 3 % Gaussian noise added in the synthetic data, the reconstructed absorption image also presents some artifacts in the inner layer.

Reconstructed images for this two-layered domain case with edge-preserving regularization incorporating structural information are shown in Figs. 4, 5 and 6. Figure 4 presents images reconstructed with perfect a priori discontinuity or edge information incorporated into edge-preserving regularization. The perfect a priori edge information means that the discontinuity between fatty, fibro-glandular, and tumor could be obtained from structural image without error. In the *first* case of reconstruction with a priori information, the simulated structural image is shown in Fig. 4a where the distribution is equivalent to the Fig. 1a, c. The bright region in Fig. 4c displays the perfect edge corresponding to the discontinuities in the structural image of Fig. 4a. This edge information could be easily acquired due to homogeneous characteristics of fatty, fibro-glandular, and tumor region in the simulated structural image. Therefore, we could incorporate this derived edge information into edge-preserving regularization by reducing the weight value b relative to this edge position with Eq. (10) at each reconstruction step, where we chose $w_b = 0.1$. Otherwise, the weight value at the dark region of Fig. 4c is increased with $w_b = 1.9$. The absorption and reduced scattering images reconstructed with edge-preserving regularization incorporating structural information are shown in Fig. 4b, d, respectively. As can be seen, Fig. 4b demonstrates a considerable improvement in the reconstructed absorption image when structural information was invoked. Moreover, artifacts previously shown in the inner layer when reconstructed with EPR were significantly eliminated.

In the *second* case of reconstruction with a priori information, we considered that the tumor is even not differentiated from the fibro-glandular in the structural image. The simulated structural image representing this situation is shown in Fig. 5a, where only fatty (outer layer) and fibro-glandular (inner layer) are present. Figure 5c shows the edge

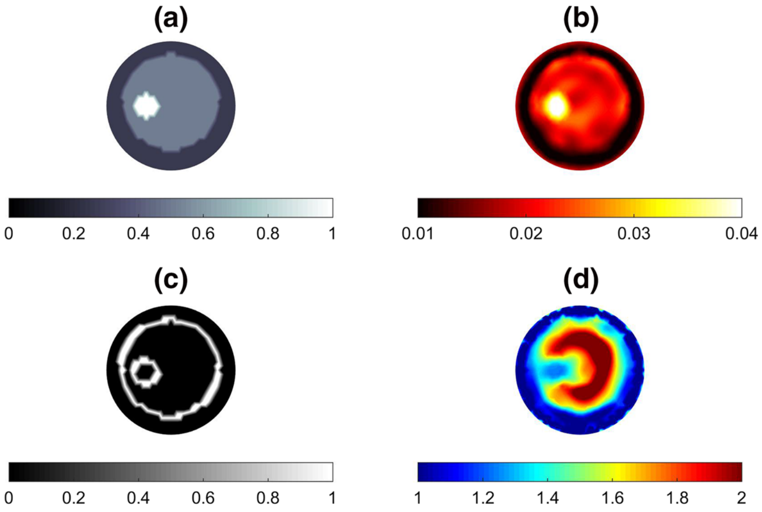

Fig. 4 Reconstruction of absorption and reduced scattering images for a phantom of layered domain with an inside inclusion through edge-preserving regularization incorporating perfect edge information. **a** Simulated structural information with an inside tumor, **b** reconstructed absorption image, **c** edge information computed from structural information (given by **a**), **d** reconstructed reduced scattering image

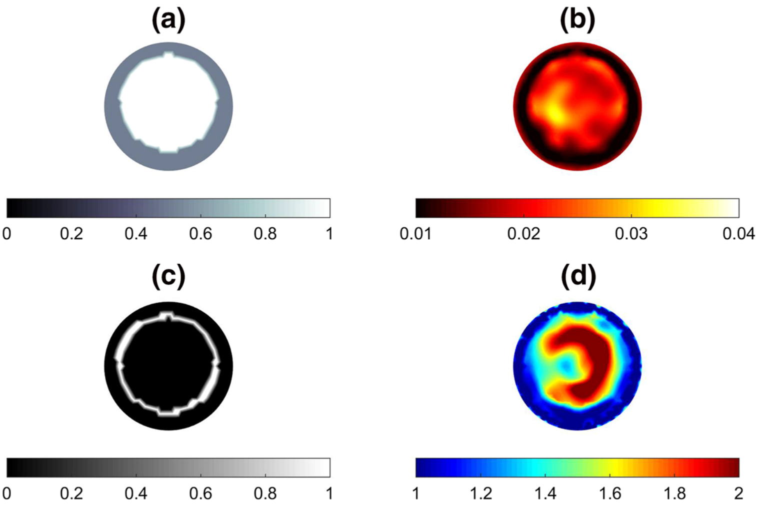

Fig. 5 Same caption as Fig. 4 except the employed structural image (as **a**) showing no tumor information

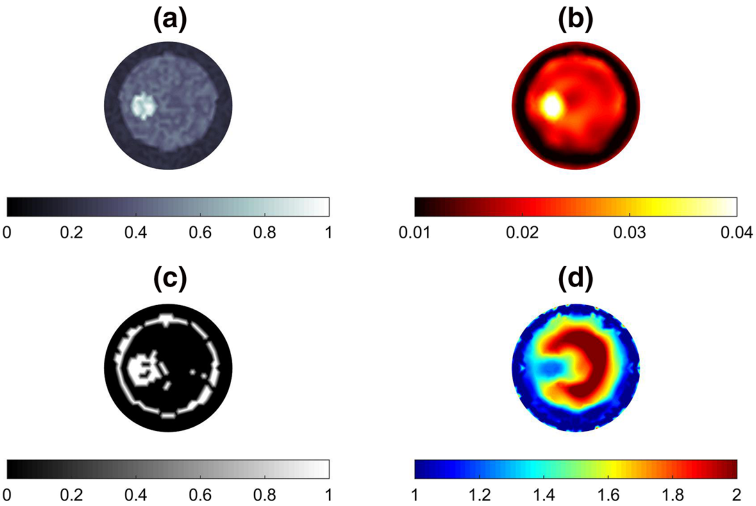

Fig. 6 Same caption as Fig. 4 except the employed imperfect structural image with added Gaussian noise

information derived from Fig. 5a. Again, during each reconstruction step, the weight value b at bright region of Fig. 5c is reduced with $w_b = 0.1$ and at dark region is increased with $w_b = 1.9$. Figure 5b, c present the absorption and reduced scattering images reconstructed with edge-preserving regularization incorporating this imperfect a priori edge information, i.e., edge of tumor could not be seen in the structural image and not utilized in the reconstruction. Clearly presented in the Fig. 5b, artifacts in inner layer had been suppressed as compared to the Fig. 3b and tumor can be reconstructed although a priori information used in reconstruction only contains edge information that separates the fatty and fibro-glandular part in structural image.

In the *third* case of reconstruction with a priori information, we considered more practical situation that the structural image obtained from other imaging modality might contain some noise or variation in the images as displayed in Fig. 6a. Due to this variation in the structural image, the edge information obtained under this condition is displayed in Fig. 6c and would not as well as the one shown in Fig. 4c. Also, the weight value b at bright region of Fig. 6c is reduced with $w_b = 0.1$ and at dark region is increased with $w_b = 1.9$ during each reconstruction step. Figure 6b, d show the reconstructed absorption and reduced scattering images with imperfect a priori edge information incorporated. As compared to the Fig. 4b, d, there is no significant difference in the reconstructed images regardless of perfect or imperfect a priori edge information used.

3.3 Reconstructions from synthesized data added with varied levels of noise

The reconstruction algorithm described in Sect. 2 are used to reconstruct images from synthesized data with 1, 3, 5, and 10 % Gaussian distributed noise to see the effect of different data noise level. The phantom geometry and the optical properties were the same to the previous section (Fig. 3a, c). Moreover, perfect spatial priors were used when edge-preserving regularization incorporating structural information.

Figure 7 displays the reconstructed absorption and reduced scattering images using edge-preserving regularization, without incorporation of structural information, and simulated data with different level of noise added. Obviously, increasing the data noise level in the simulated data significantly affects the reconstructed absorption images. Without structural priors, inclusion in the inner layer still could be reconstructed. However, the

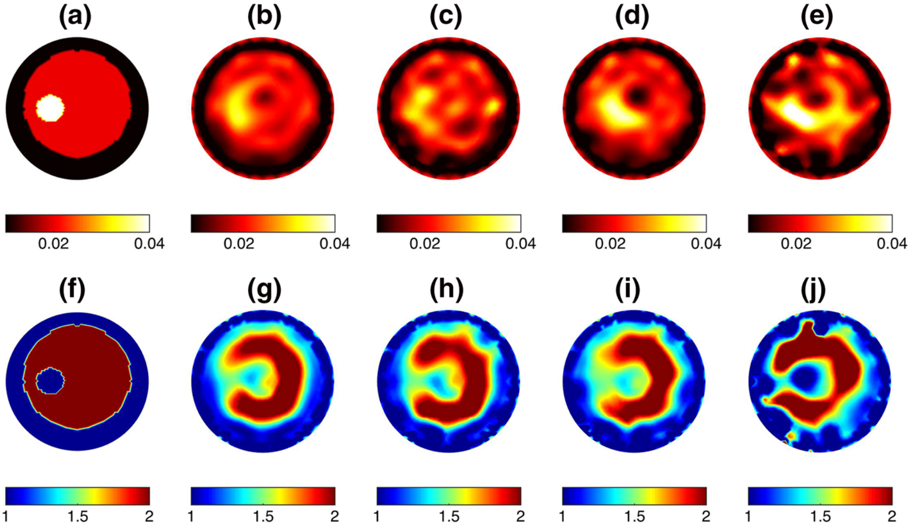

Fig. 7 Demonstration of reconstructed absorption and reduced scattering images using synthesized data added with varied levels of noise and edge-preserving regularization, *without* structural image available. **a** designated absorption coefficient distribution, reconstructed absorption images from synthesized data added with **b** 1 %, **c** 3 %, **d** 5 % and **e** 10 % noise; **f** designated reduced scattering coefficient distribution, and reconstructed reduced scattering images from synthesized data added with **g** 1 %, **h** 3 %, **i** 5 % and **j** 10 % noise

shape of the inclusion is distorted notably especially when 5 and 10 % noise added in the data as present in Fig. 7d, e.

In contrast to Fig. 7, Fig. 8 shows that, with structural priors, increasing the data noise level in the simulated data did not significantly affect the reconstructed images. Moreover, with the help of a priori information, the shape of the inclusion in the reconstructed absorption images is close to the exact one as shown in Fig. 8a. This is due to the reason that using proper weight value b allows noise or artifact elimination and edge preservation during the reconstruction, where we increased or reduced the weight value depending on the edge information derived from structural image.

3.4 Reconstruction from experimental data

In this section, our proposed EPR incorporating structural information was justified using experimental data. A 50-mm-diameter cylindrical phantom, composed of fat emulsion suspension (Lipovenoes) as the scattering medium and ink as the absorber, was made with background optical properties of $\mu_a = 0.006\ \text{mm}^{-1}$ and $\mu_s' = 0.6\ \text{mm}^{-1}$. The 830 nm NIR light source with the power of 7 mW was used during measurement.

Figure 9a, b display the images reconstructed from the conventional EPR and EPR incorporating structural information, respectively, with the experimental data collected from the phantom with an eccentrically located 10-mm-diameter inclusion (12.5 mm off center along the horizontal axis at 180°) having a 4:1 contrast level with respect to the background medium. Figure 9c, d illustrate one-dimensional (1D) circular profiles through the center of the inclusion at radius of 12.5 mm. As demonstrated in Fig. 9b, artifact around the boundary of μ_s' image can be reduced when structural information was utilized into EPR algorithm. Moreover, the shape of the inclusion is preserved as indicated in Fig. 9d.

Figure 10 demonstrates the reconstruction of two eccentrically located inclusions having 4:1 contrast level with respect to the background medium. Similar to the previous

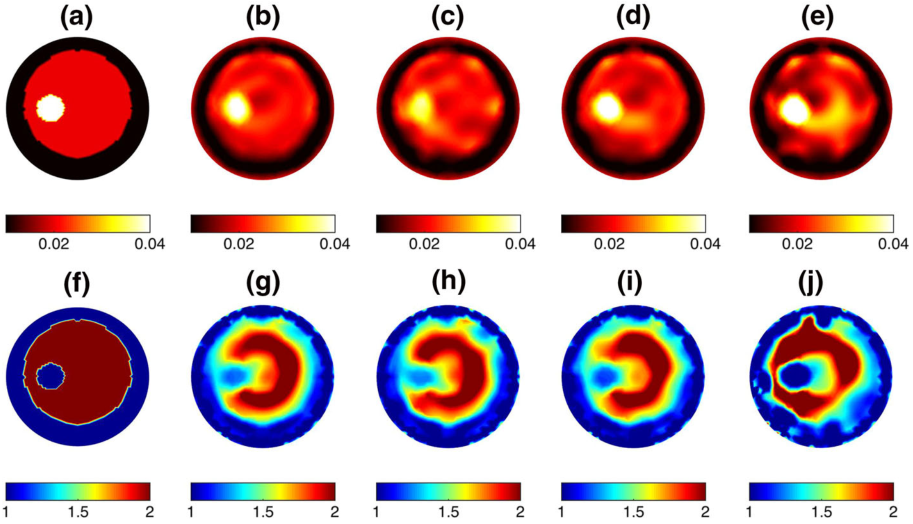

Fig. 8 Same caption as Fig. 7 except *with* structural image available for edge-preserving regularization

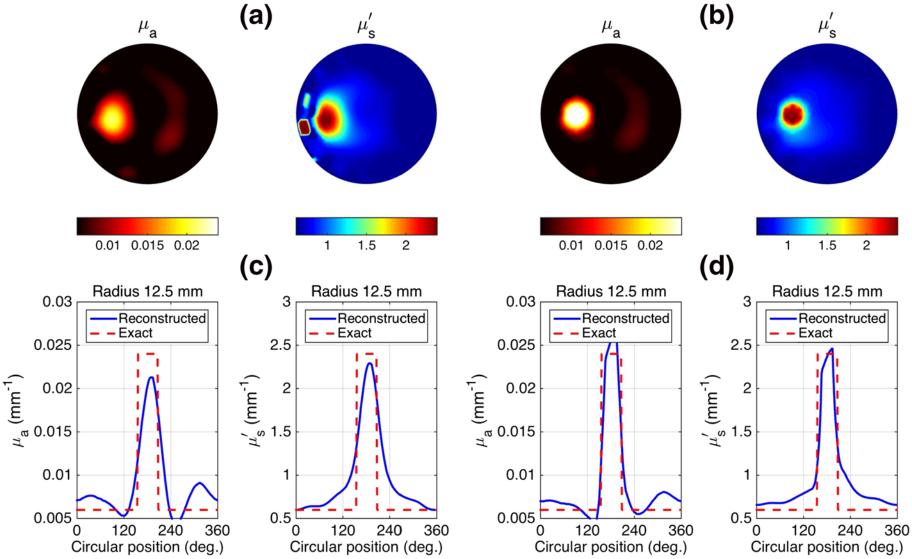

Fig. 9 Reconstruction from experimental data obtained from an eccentrically located inclusion with a contrast of four for both μ_a and μ_s'. **a**, **b** are the reconstructed μ_s' and μ_s' images through using conventional edge-preserving regularization and edge-preserving regularization with structural information, respectively; **c**, **d** are the 1D circular profiles cutting through the images of **a** and **b**

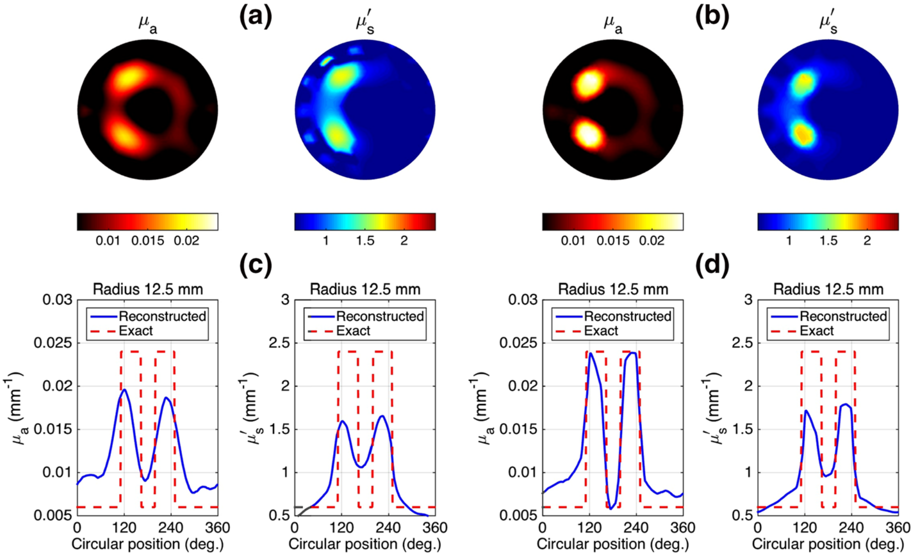

Fig. 10 Same caption as Fig. 9 except reconstruction from experimental data obtained from two eccentrically located inclusions having a 4:1 contrast level with respect to the background medium

reconstruction results, artifact around the boundary of reconstructed μ_s' image can be diminished, and the shape of inclusions were maintained significantly when reconstructed from EPR with structural information, as shown in Fig. 10b, d.

4 Conclusions

In this study, we have presented an image reconstruction algorithm using modified EPR scheme incorporating with a priori structural information. The auxiliary variable *b*, which is introduced to linearize the minimization problem in EPR, marks the location of discontinuities. That provides the rationale for us to modify the auxiliary variable during each reconstruction step according to the a priori edge information obtained from the structural image. Three varied scenarios are presented to verify the robustness of proposed algorithm with respect to the accuracy and availability of a priori edge information. In the second scenario the tumor can still be characterized even though it is not available and shown in the structural image; further, in scenario 3, the proposed scheme shows its robustness, not affected by the inaccuracy and incorrectness of edge information. These cases demonstrate that the incorporated a priori edge information further enable improving the DOI image reconstruction. Besides, the reconstruction using noisy data sets shows its merits in the real situations as the measured data are usually corrupted by the noise.

Acknowledgments This research was financially supported by the Ministry of Science and Technology in Taiwan through Grants 101-2221-E-008-010-MY2, 101-2221-E-008-093-MY3, and 101-2221-E-236-014.

References

Azar, F.S., Lee, K., Khamene, A., Choe, R., Corlu, A., Konecky, S.D., Sauer, F., Yodh, A.G.: Standardized platform for coregistration of nonconcurrent diffuse optical and magnetic resonance breast images obtained in different geometries. J. Biomed. Opt. **12**, 051902 (2007)

Boverman, G., Miller, E.L., Li, A., Zhang, Q., Chaves, T., Brooks, D.H., Boas, D.A.: Quantitative spectroscopic diffuse optical tomography of the breast guided by imperfect a priori structural information. Phys. Med. Biol. **50**, 3941–3956 (2005)

Brooksby, B., Jiang, S., Dehghani, H., Pogue, B.W., Paulsen, K.D., Kogel, C., Doyley, M., Weaver, J.B., Poplack, S.P.: Magnetic resonance-guided near-infrared tomography of the breast. Rev. Sci. Instrum. **75**, 5262–5270 (2004)

Brooksby, B., Jiang, S., Dehghani, H., Pogue, B.W., Paulsen, K.D., Weaver, J., Kogel, C., Poplack, S.P.: Combining near-infrared tomography and magnetic resonance imaging to study in vivo breast tissue: implementation of a Laplacian-type regularization to incorporate magnetic resonance structure. J. Biomed. Opt. **10**, 051504 (2005)

Brooksby, B., Pogue, B.W., Jiang, S., Dehghani, H., Srinivasan, S., Kogel, C., Tosteson, T.D., Weaver, J., Poplack, S.P., Paulsen, K.D.: Imaging breast adipose and fibroglandular tissue molecular signatures by using hybrid MRI-guided near-infrared spectral tomography. Proc. Natl. Acad. Sci. U.S.A. **103**, 8828–8833 (2006)

Cerussi, A., Shah, N., Hsiang, D., Durkin, A., Butler, J., Tromberg, B.J.: In vivo absorption, scattering, and physiologic properties of 58 malignant breast tumors determined by broadband diffuse optical spectroscopy. J. Biomed. Opt. **11**, 044005 (2006)

Chen, N.G., Guo, P., Yan, S., Piao, D., Zhu, Q.: Simultaneous near-infrared diffusive light and ultrasound imaging. Appl. Opt. **40**, 6367–6380 (2001)

Chen, L.Y., Pan, M.C., Pan, M.C.: Implementation of edge-preserving regularization for frequency-domain diffuse optical tomography. Appl. Opt. **51**, 43–54 (2012)

Chen, L.Y., Pan, M.C., Pan, M.C.: Flexible near-infrared diffuse optical tomography with varied weighting functions of edge-preserving regularization. Appl. Opt. **52**, 1173–1182 (2013)

Choe, R., Konecky, S.D., Corlu, A., Lee, K., Durduran, T., Busch, D.R., Pathak, S., Czerniecki, B.J., Tchou, J., Fraker, D.L., DeMichele, A., Chance, B., Arridge, S.R., Schweiger, M., Culver, J.P., Schnall, M.D., Putt, M.E., Rosen, M.A., Yodh, A.G.: Differentiation of benign and malignant breast tumors by in vivo three-dimensional parallel-plate diffuse optical tomography. J. Biomed. Opt. **14**, 024020 (2009)

Collettini, F., Martin, J.C., Diekmann, F., Fallenberg, E., Engelken, F., Ponder, S., Kroencke, T.J., Hamm, B., Poellinger, A.: Diagnostic performance of a near-infrared breast imaging system as adjunct to mammography versus X-ray mammography alone. Eur. Radiol. **22**, 350–357 (2012)

Durduran, T., Choe, R., Baker, W.B., Yodh, A.G.: Diffuse optics for tissue monitoring and tomography. Rep. Prog. Phys. **73**, 076701 (2012)

Elmore, J.G., Barton, M.B., Moceri, V.M., Polk, S., Arena, P.J., Fletcher, S.W.: Ten-year risk of false positive screening mammograms and clinical breast examinations. N. Engl. J. Med. **338**, 1089–1096 (1998)

Fang, Q., Carp, S.A., Selb, J., Boverman, G., Zhang, Q., Kopans, D.B., Moore, R.H., Miller, E.L., Brooks, D.H., Boas, D.A.: Combined optical imaging and mammography of the healthy breast: optical contrast derived from breast structure and compression. IEEE Trans. Med. Imaging **28**, 30–42 (2009)

Fang, Q., Selb, J., Carp, S.A., Boverman, G., Miller, E.L., Brooks, D.H., Moore, R.H., Kopans, D.B., Boas, D.A.: Combinded optical and X-ray tomosynthesis breast imaging. Radiology **258**, 89–97 (2011)

Fantini, S., Sassaroli, A.: Near-infrared optical mammography for breast cancer detection with intrinsic contrast. Ann. Biomed. Eng. **40**, 398–407 (2012)

Huynh, P.T., Jarolimek, A.M., Day, S.: The false-negative mammogram. Radiographics **18**, 1137–1154 (1998)

Hylton, N.: Magnetic resonance imaging of the breast: opportunities to improve breast cancer management. J. Clin. Oncol. **23**, 1678–1684 (2005)

Kolb, T.M., Lichy, J., Newhouse, J.H.: Comparison of the performance of screening mammography, physical examination and breast US and evaluation of factors that influence them: an analysis of 27,825 patient evaluations. Radiology **225**, 165–175 (2002)

Krishnaswamy, V., Michaelsen, K.E., Pogue, B.W., Poplack, S.P., Shaw, I., Defrietas, K., Brooks, K., Paulsen, K.D.: A digital X-ray tomosynthesis coupled near-infrared spectral tomography system for dual-modality breast imaging. Opt. Express **20**, 19125–19136 (2012)

Li, A., Miller, E.L., Kilmer, M.E., Brukilacchio, T.J., Chaves, T., Stott, J., Zhang, Q., Wu, T., Chorlton, M., Moore, R.H., Kopans, D.B., Boas, D.A.: Tomographic optical breast imaging guided by three-dimensional mammography. Appl. Opt. **42**, 5181–5190 (2003)

Michaelsen, K., Krishnaswamy, V., Pogue, B.W., Poplack, S.P., Paulsen, K.D.: Near-infrared spectral tomography integrated with digital breast tomosynthesis: effects of tissue scattering on optical data acquisition design. Med. Phys. **39**, 4579–4587 (2012)

Nothacker, M., Duda, V., Hahn, M., Warm, M., Degenhardt, F., Madjar, H., Weinbrenner, S., Albert, U.-S.: Early detection of breast cancer: benefits and risks of supplemental breast ultrasound in asymptomatic women with mammographically dense breast tissue. A systematic review. BMC Cancer **9**, 335 (2009)

Tabar, L., Yen, M.F., Vitak, B., Chen, H.T., Smith, R.A., Duffy, S.W.: Mammography service screening and mortality in breast cancer patients: 20-year follow-up before and after introduction of screening. Lancet **361**, 1405–1410 (2003)

World Health Organization. Cancer Fact Sheet No. 297. Technical report (2015)

Yalavarthy, P.K., Pogue, B.W., Dehghani, H., Carpenter, C.M., Jiang, S., Paulsen, K.D.: Structural information within regularization matrices improves near infrared diffuse optical tomography. Opt. Express **15**, 8043–8058 (2007)

Zhao, Y., Mastanduno, M.A., Jiang, S., Ghussein, F., Gui, J., Pogue, B.W., Paulsen, K.D.: Optimization of image reconstruction for magnetic resonance imaging-guided near-infrared diffuse optical spectroscopy in breast. J. Biomed. Opt. **20**, 056009 (2015)

Zhu, Q., Chen, N.G.: Imaging tumor angiogenesis by use of combined near-infrared diffusive light and ultrasound. Opt. Lett. **28**, 337–339 (2003)

Zhu, Q., Durdurna, T., Ntziachristos, V., Holboke, M., Yodh, A.G.: Imager that combines near-infrared diffusive light and ultrasound. Opt. Lett. **24**, 1050–1052 (1999)

Zhu, Q., Tannenbaum, S., Hegde, P., Kane, M., Xu, C., Kurtzman, S.H.: Noninvasive monitoring of breast cancer during neoadjuvant chemotherapy using optical tomography with ultrasound localization. Neoplasia **10**, 1028–1040 (2008)